SPECIAL ISSUE

CSIRO PUBLISHING

International Journal of Wildland Fire
http://dx.doi.org/10.1071/WF13015

Mapping the daily progression of large wildland fires using MODIS active fire data

Sander Veraverbeke[A,B,D], *Fernando Sedano*[B,C], *Simon J. Hook*[A], *James T. Randerson*[B], *Yufang Jin*[B] *and Brendan M. Rogers*[B]

[A]Jet Propulsion Laboratory (NASA), California Institute of Technology, 4800 Oak Grove Drive, Pasadena, CA 91109, USA.
[B]Department of Earth System Science, University of California, 2224 Croul Hall, Irvine, CA 92697, USA.
[C]Department of Geograpical Sciences, University of Maryland, 2181 LeFrak Hall, College Park, MD 20742, USA.
[D]Corresponding author. Email: sander.veraverbeke@uci.edu

Abstract. High temporal resolution information on burnt area is needed to improve fire behaviour and emissions models. We used the Moderate Resolution Imaging Spectroradiometer (MODIS) thermal anomaly and active fire product (MO(Y)D14) as input to a kriging interpolation to derive continuous maps of the timing of burnt area for 16 large wildland fires. For each fire, parameters for the kriging model were defined using variogram analysis. The optimal number of observations used to estimate a pixel's time of burning varied between four and six among the fires studied. The median standard error from kriging ranged between 0.80 and 3.56 days and the median standard error from geolocation uncertainty was between 0.34 and 2.72 days. For nine fires in the south-western US, the accuracy of the kriging model was assessed using high spatial resolution daily fire perimeter data available from the US Forest Service. For these nine fires, we also assessed the temporal reporting accuracy of the MODIS burnt area products (MCD45A1 and MCD64A1). Averaged over the nine fires, the kriging method correctly mapped 73% of the pixels within the accuracy of a single day, compared with 33% for MCD45A1 and 53% for MCD64A1. Systematic application of this algorithm to wildland fires in the future may lead to new information about vegetation, climate and topographic controls on fire behaviour.

Additional keywords: carbon emissions, fire growth, fire propagation, fire spread.

Received 30 January 2013, accepted 12 November 2013, published online 7 March 2014

Introduction

Landscape fires release large amounts of particulate matter and trace gases into the atmosphere, and global estimates of carbon emissions from fires range between 1500 and 3500 Tg carbon per year (van der Werf *et al.* 2010). On a regional scale, wildfire emissions affect air quality and air pollution, which can have adverse effects on public health, especially when the wildfire emissions disperse into densely populated areas (Cisneros *et al.* 2012; Johnston *et al.* 2012). Existing bottom-up inventories for wildfire emissions traditionally assess emissions from individual fires using maps of the final outer perimeter, average over multiple fire perimeters in large areas (e.g. the Wildland Fire Emission Information System, French *et al.* 2011) or have coarse spatial resolutions (e.g. 0.5° in the Global Fire Emission Database version 3 (GFED3), van der Werf *et al.* 2010). As a consequence, these models may not be able to capture day-to-day variation in weather and fuel moisture during fire events, which in turn may bias estimates of combustion completeness and emission factors (Boschetti *et al.* 2010; van Leeuwen and van der Werf 2011), and propagate into larger emissions uncertainties. For example, Mu *et al.* (2011) demonstrated that refining the temporal resolution of GFED3 from monthly to daily time intervals reduces uncertainties in modelling the contribution of wildfire emissions to atmospheric trace gases.

Space-borne sensors with short revisit times have been shown to be well suited to providing temporal information on wildfire occurrence and progression (Chuvieco and Martin 1994; Loboda and Csiszar 2007; Mu *et al.* 2011). In particular, measurements from satellites in geostationary and non-sun synchronous low earth orbits have been used to study the diurnal pattern of biomass burning (Prins *et al.* 1998; Giglio 2007). These studies generally count the total number of fire pixels over large areas at discrete time steps to assess the pattern of the diurnal fire cycle. Although the short revisit time of geostationary satellites allows high temporal detail for fire activity studies, the spatial resolution of these satellites is inadequate to monitor the evolution of individual fire events. The Moderate Resolution Imaging Spectroradiometer (MODIS) has become one of the primary instruments for moderate-resolution fire remote sensing since it was launched on the Terra satellite in 1999 and on Aqua in 2002

(Justice *et al.* 2002). At the equator, MODIS has four daily overpasses: at 0130 hours (Aqua descending node), 1030 hours (Terra descending node), 1330 hours (Aqua ascending node) and 2230 hours (Terra ascending node), local times. Owing to the curvature of the earth, the number of MODIS acquisitions each day at a specific location increases with latitude. Two types of fire products are consistently generated and distributed from MODIS. These are (1) the active fire products, which give the location of the fire and fire radiative power when possible and (2) the burnt area products, which provide information about the spatial extent of burn scars (Justice *et al.* 2002). The active fire algorithm is based primarily on the detection of an increase in brightness temperatures in the MODIS 4- and 11-μm channels when fires are active (Giglio *et al.* 2003; Giglio *et al.* 2006). The standard MODIS burnt area product (Roy *et al.* 2002; Roy *et al.* 2005) makes use of post-fire reflectance changes in the near infrared (NIR) and short-wave infrared (SWIR) spectral regions. These reflectance changes are caused by the removal of vegetation and deposition of charcoal and ash by fire (Pereira *et al.* 1999; Trigg and Flasse 2001). In addition to spatial burn extent information, the algorithm also provides the approximate day of burning, with a nominal uncertainty of up to eight days (Roy *et al.* 2005). Giglio *et al.* (2009) describe another MODIS burnt area product that combines information on post-fire reflectance changes in the NIR and SWIR spectral regions with active fire detections in the thermal infrared region. Inclusion of active fire information is planned for the MODIS Collection 6 burnt area product (Giglio *et al.* 2009). As with the burnt area product of Roy *et al.* (2005), the Giglio *et al.* (2009) product also provides information on the day of burning.

Although temporal information on the day of burning has been included in both the MODIS active fire and burnt area products for many years, few studies have attempted to use this information to derive data on fire progression at local to regional scales (Loboda and Csiszar 2007; Thorsteinsson *et al.* 2011; Kasischke and Hoy 2012). At these scales, fire progression information can significantly enhance bottom-up estimates of emissions (Boschetti *et al.* 2010; Mu *et al.* 2011) and may enable analysis of the sensitivity of fire spread rates to local environmental conditions (e.g. wind speed, wind direction, relative humidity, air temperature, topography and fuel types). In this study we use kriging (Royle *et al.* 1981; Holdaway 1996), a well-accepted interpolation technique, to retrieve fire progression maps at moderate resolution scale using MODIS active fire data. We derive fire progression maps of selected large fires spanning a range of vegetation and fuel types, topography and weather. We compare our estimates of the time of burning with high-resolution fire perimeter data extracted from night-time airborne infrared acquisitions, and with the approximate day of burning provided by the MODIS burnt area products of Roy *et al.* (2005) and Giglio *et al.* (2009). The resulting fire progression maps assign the burn date within the accuracy of a single day to 73% of the pixels, noticeably outperforming accuracy of the MODIS burnt area products.

Methods

Fires included in this study

In this study, we derived the progression of 16 large wildland fires in the south-western US and Alaska (Fig. 1, Table 1). Nine

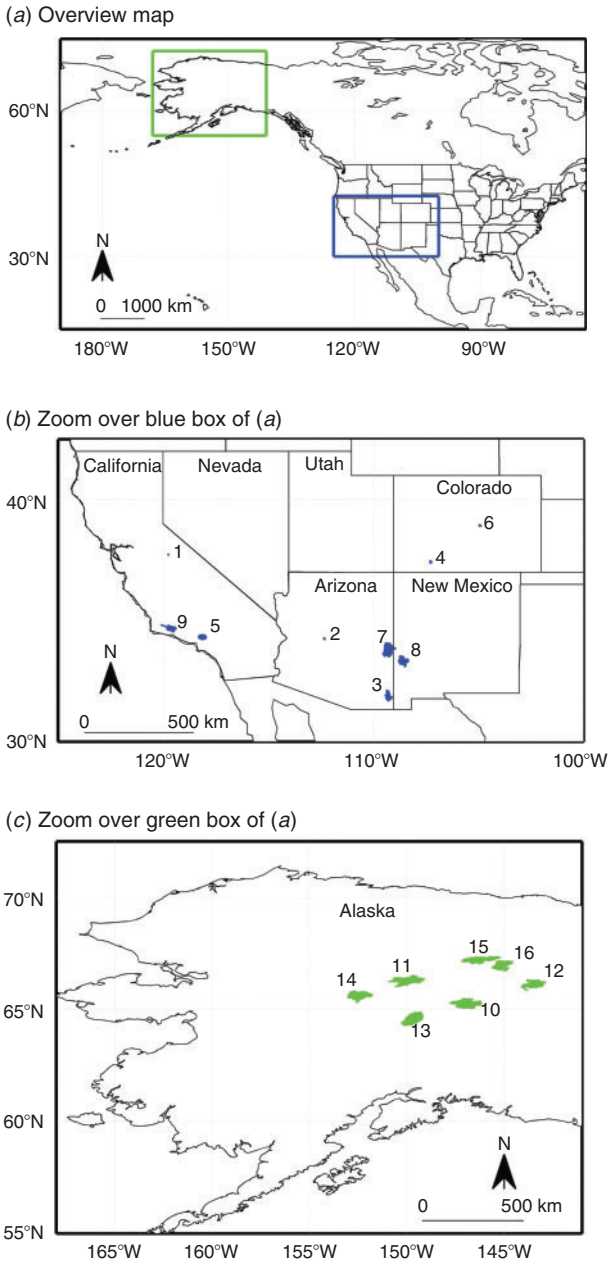

Fig. 1. Distribution of 16 large wildland fires analysed in this study. (*a*) Overview map. Fire perimeters are from the United States Forest Service (*b*) and the Alaska Large Fire Database (*c*). For detailed information on each individual fire numbered from 1 to 16 in (*b*) and (*c*), refer to Table 1.

of these wildland fires were selected because of the availability of high-resolution daily fire perimeter data derived from night-time airborne infrared imagery archived by the US Forest Service. Those nine fires, ranging between 3000 and 240 000 ha, were in California, Arizona, New Mexico and Colorado (Fig. 1*b*) and occurred between 2007 and 2012 (Table 1). We also generated progression maps for seven large fires in Alaska (Fig. 1*c*) with fire size ranging between 139 000 and 229 000 ha. Final perimeters for the Alaskan fires were available from the Alaska Large Fire Database, although daily fire perimeter data

Table 1. Large wildland fires analysed in this study

The perimeters of individual fires are shown in Fig. 1. The fires in the table are ordered alphabetically per region. The forest (classes 1–5), shrubland (classes 6–7), savanna–grassland (class 10) and other (classes 11–16) land cover types refer to aggregated classes of the International Geosphere–Biosphere Program (IGBP) vegetation classification from the MCD12Q1 land cover type product (Friedl *et al.* 2010) acquired for the year before each fire. In 'Missing days in daily fire perimeter data', dashes indicate that there were no missing days. Note that for savanna–grassland the MCD12Q1 product has difficulties in discriminating between open forest, shrubland and savanna (http://landweb.nascom.nasa.gov/cgi-bin/QA_WWW/displayCase.cgi?esdt=MCD12andcaseNum=PM_MCD12_11001andcaseLocation=cases_data, accessed 21 October 2013). For the fires in southern California the MCD12Q1 classification as savanna largely corresponds with chaparral shrubland. Similarly, the MCD12Q1 classification as savanna in Alaska largely corresponds with an open taiga forest interspersed with herbaceous tundra species and shrubs

Region Fire name	State	Size (ha)	Year	Days of the year	Land cover types (%)				Fire number in Fig. 1	Missing days in daily fire perimeter data
					Forest	Shrubland	Savanna–grassland	Other		
South-west										
Big Meadow	CA	3001	2009	239–249	49	0	44	7	1	–
Gladiator	AZ	6566	2012	135–145	8	53	39	0	2	–
Horseshoe	AZ	90 269	2011	129–171	3	51	44	2	3	–
Little Sand	CO	10 087	2012	145–184	99	0	1	0	4	181, 182, 184
Station	CA	64 425	2009	239–261	9	24	66	1	5	–
Waldo Canyon	CO	7390	2012	175–183	48	0	49	3	6	–
Wallow	AZ–NM	217 742	2011	150–177	65	13	19	3	7	–
Whitewater Baldy	NM	120 055	2012	135–172	42	25	31	2	8	–
Zaca	CA	239 973	2007	186–238	8	21	71	0	9	206–208
Alaska										
Boundary	AK	226 847	2004	171–240	4	13	81	2	10	N/A
Dall City	AK	205 247	2004	191–257	1	22	75	2	11	N/A
Little Black One	AK	146 064	2009	174–220	23	13	63	1	12	N/A
Minto Flats South	AK	228 577	2009	172–218	44	22	34	0	13	N/A
North Dag	AK	180 104	2004	167–239	2	6	37	1	14	N/A
Pingo	AK	169 429	2004	168–257	5	15	79	1	15	N/A
Wintertrail	AK	139 012	2004	170–261	1	8	82	0	16	N/A

were not available. In higher latitudes, the number of MODIS acquisitions per day increases, which allowed for a complementary analysis of the uncertainties in the progression model. Five of the Alaskan fires occurred in 2004 and the other two in 2009 (Table 1). We used the MODIS land cover type product (MCD12Q1, Friedl *et al.* 2010) of the year before each fire with the International Geosphere–Biosphere Program (IGBP) classification scheme to quantify pre-fire land cover conditions (http://reverb.echo.nasa.gov, accessed 21 October 2013). We combined the original land cover classes into between forest (classes 1–5), shrubland (classes 6–7), savanna–grassland (classes 8–10) and other aggregated vegetation types (classes 11–16). The fires in our analysis occurred in many of these vegetation types (Table 1).

Daily fire perimeter data

Daily perimeter data from the fires in the south-west were obtained from the National Interagency Fire Center (ftp://ftp.nifc.gov, accessed 21 October 2013). Trained ground fire personnel created these fire perimeter data by manually interpreting and digitising high resolution (1 m with sub-pixel geolocation accuracy) night-time infrared imagery from the USFS National Infrared Operations (NIROPS, http://nirops.fs.fed.us/, accessed 21 October 2013) in which the active fire front is visible. The acquisition time of the infrared imagery was mostly close to midnight (between 2200 and 0200 hours), but did vary more in some cases. The temporal uncertainty introduced from the different sampling intervals of the night-time infrared imagery is likely to be small as fire spread rates and fire activity are significantly lower during the night compared with during the day (Prins *et al.* 1998; Giglio 2007; Mu *et al.* 2011). In a final step, the daily fire perimeter vector data were used to construct a single map of daily fire progression. As described below, these observations were used to validate the fire progression model we developed using MODIS active fire data and to compare with estimates from available global-scale MODIS burnt area products.

MODIS active fire data

We used the timing and locations of the Terra and Aqua thermal anomalies and fire 5-min (1-km) products (MOD14 and MYD14) to construct the fire progression model (http://reverb.echo.nasa.gov, accessed 21 October 2013). The MODIS active fire data were extracted to cover each of the fire perimeters from 1 month before until 1 month after the respective start and end dates of each individual fire as defined using the USFS observation described above. The MOD14 and MYD14 products are based on a contextual active fire detection algorithm that exploits the strong emission in the mid infrared spectral region from fires (Giglio *et al.* 2003, 2006). Active fire pixels are categorised as having low, medium or high confidence levels of fire detection. We used all confidence levels in our study.

MODIS burnt area products

We compared the daily progression observations with the dates of burning reported by two types of MODIS burnt area products,

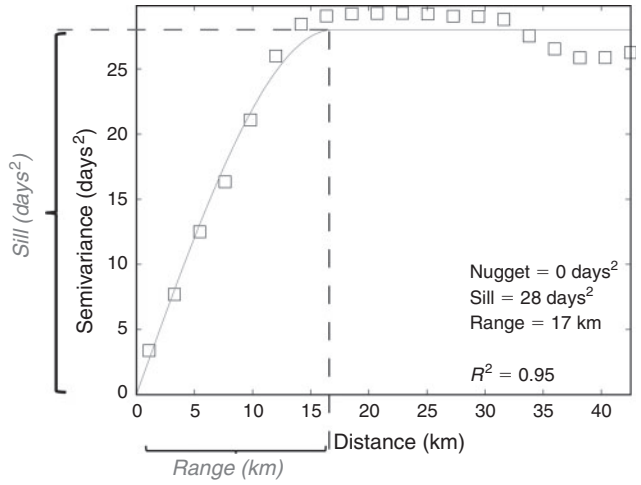

Fig. 2. Example variogram of the 2011 Wallow fire in Arizona and New Mexico. The semi-variance was calculated for different distance bins (squares). A spherical model was used to describe and parameterise the model. The range is the distance at which the model levels out. The semi-variance value at which the variogram attains the range is called the sill. The semi-variance value at which the variogram fit crosses the *y*-axis is called the nugget (in the example of the Wallow fire, the nugget is 0 days^2).

both at 500-m resolution. The combined MODIS Terra and Aqua monthly burnt area product (500 m) (MCD45A1) was also retrieved from the Reverb website (http://reverb.echo.nasa.gov, accessed 21 October 2013) for all nine fires in the south-west from at least 1 month before until at least 1 month after the fire (with the temporal window defined by the day of the first and last active fire observed within the final fire perimeter). This product provides monthly gridded burnt area data. The algorithm is based on the spectral and temporal changes in surface reflectance that fires induce (Roy *et al.* 2005). A statistical measure is applied on the NIR and SWIR reflectance changes to select potential burnt pixels. Subsequently, a temporal constraint eliminates temporary changes such as those due to shadow effects, and an approximate day of burning is assigned to burnt pixels. To incorporate uncertainties due to missing data (mostly from cloudy observations) the approximate day of burning is assigned with a nominal uncertainty of 8 days (Roy *et al.* 2005).

The combined MODIS Terra and Aqua direct broadcast monthly burnt area product (500 m) (MCD64A1) was also obtained for all nine fires in the south-west from at least 1 month before until at least 1 month after the fire (ftp://fuoco.geog.umd.edu, accessed 21 October 2013). Similar to MCD45A1, this product also applies thresholds on temporal changes in a burn-sensitive vegetation index to detect areas burnt along with the approximate day of burning (Giglio *et al.* 2009). In contrast to MCD45A1, MCD64A1 incorporates cumulative active fire maps to guide the selection of burnt and unburnt training samples for the change detection algorithm (Giglio *et al.* 2009).

Modelling fire progression using kriging

Due to the curvature of the earth, the number of MODIS acquisitions per day increases with latitude, and as a consequence the temporal gaps between successive overpasses become smaller with increasing latitude. However, due to cloud and smoke cover, the timing and number of acquisitions, heterogeneity in fuel loads and weather-driven variations in fire spread rates, the spatial pattern of the detected active fires within a fire complex is discontinuous. We used ordinary kriging to derive spatially continuous maps of the time of burning. Kriging is a geostatistical interpolation technique that calculates values at unknown locations based on a scattered set of known locations. The technique has been widely used to predict continuous maps of a wide range of environmental variables (e.g. precipitation, elevation, frost, air temperature) based on discontinuous point data (e.g. Holdaway 1996; Schwendel *et al.* 2012). The values at unknown locations are calculated based on a combination of the distance to the known locations and the spatial arrangement of the known locations. A major advantage of kriging compared with deterministic interpolation methods such as inverse distance weighting is that kriging allows the interpolation error to be quantified (Holdaway 1996). The spatial arrangement of the known locations is quantified by fitting variogram curves. A variogram describes the spatial variability of a specific environmental variable and is modelled using the range, sill and nugget parameters (Fig. 2). The range is the distance after which the model flattens. This means that there is no spatial autocorrelation effect beyond this distance. The value at which the variogram model attains the range is called the sill. The nugget is the value where the curve crosses the *y*-axis. A nugget larger than zero means that observations at infinitely small distances show a discontinuity. We fitted spherical models for each fire separately to derive the range, sill and nugget as input to the kriging interpolation. The variogram and spherical curve fit for the Wallow fire are shown in Fig. 2. The progression maps were derived in fractional days from the MODIS active fire data. The times of burning for all fire pixels identified by the MO(Y)D14 product were overlaid on a georeferenced map using the day and local time of the active fire detection. As such, sub-daily estimates of time of burning were given by the kriging method. We performed an additional analysis to determine the number of observations (n) to be used to calculate the unknown locations for each fire separately. We determined the final number of observations included in the interpolation (n) as the number at which the decrease in the median kriging error became small and was less than 1% compared with the median kriging error when $n+1$ observations were included. The kriging interpolation was bound within the final fire perimeter and the interpolated time of burning was gridded at 500-m resolution to facilitate comparison with the MCD45A1 and MCD64A1 products. We also performed an additional analysis to quantify possible interpolation errors due to geolocation uncertainties in the MO(Y)D14 product. Depending on fire temperature, only 1–10% of the pixel area has to experience an elevated temperature in order to be detected using the active fire algorithm (Giglio *et al.* 2003). Thus, the active fire front only takes up part of the pixel area and can be located at any sub-pixel location. However, the area of a pixel is nominally 1 km^2 at nadir, although it grows away from nadir as the product of the along-scan (S) and along-track pixel dimension (T) (Ichoku and Kaufman 2005). At the edge of a scene, at view zenith angles of 55°, S is ~5 km and T is ~2 km (Ichoku and Kaufman 2005). The sub-pixel location uncertainty of the fire location introduces uncertainty in the kriging model. We calculated S and T for each

Table 2. Kriging parameters and the first quartile (Q1), median (Q2) and third quartile (Q3) of the kriging standard error and the standard error due to potential geolocation errors in the MO(Y)14 product

n is the number of observations included to calculate a pixel's value

Region	Kriging parameters					Kriging standard error (days)			Standard error due to geolocation error (days)		
Fire name	Nugget ($days^2$)	Sill ($days^2$)	Range (km)	R^2	*n*	Q_1	Q_2	Q_3	Q_1	Q_2	Q_3
South-west											
Big Meadow	0	15	8	0.91	4	0.85	0.92	1.01	0.69	1.01	1.32
Gladiator	0	11	9	0.96	5	0.81	0.89	0.96	0.62	0.89	1.16
Horseshoe	0	273	40	0.98	5	1.30	1.43	1.56	0.66	1.04	2.00
Little Sand	0	110	6	0.95	4	1.64	1.81	2.01	1.74	2.72	4.49
Station	0.27	11	35	0.93	5	0.84	0.87	0.91	0.24	0.34	0.53
Waldo Canyon	0	2	4	0.85	4	0.73	0.80	0.90	0.21	0.45	0.82
Wallow	0	28	17	0.95	4	0.93	1.03	1.15	0.47	0.82	1.29
Whitewater Baldy	0.47	34	17	0.97	5	1.10	1.16	1.23	0.57	0.92	1.37
Zaca	0	411	76	0.86	5	1.18	1.28	1.39	0.35	0.69	1.36
Alaska											
Boundary	12.84	334	26	0.97	5	2.19	2.26	2.36	0.48	0.95	2.02
Dall City	0	158	12	0.67	5	1.50	1.67	1.84	0.48	1.03	3.25
Little Black One	2.85	128	15	0.78	5	1.62	1.70	1.80	1.05	2.04	3.30
Minto Flats South	0	132	33	0.97	5	1.14	1.27	1.40	0.68	1.30	2.37
North Dag	0	612	64	0.96	5	1.53	1.70	2.00	0.49	0.88	2.53
Pingo	31.00	857	47	0.99	5	2.60	2.65	2.73	0.96	1.93	4.13
Wintertrail	134.00	333	34	0.94	6	3.55	3.56	3.57	0.67	1.96	4.46

fire pixel following the formulae of Ichoku and Kaufman (2005). We then calculated the maximal possible geolocation error V on the location active fire front as half the pixel diagonal $V = \sqrt{S^2 + T^2}/2$. Then, we simulated 10 sets of geolocation errors in x and y by multiplying V with values derived from a normal distribution with a mean of zero and standard deviation (s.d.) of one for each fire. These sets of geolocation errors were added to the x and y coordinates of the MODIS active fire observations. We then executed the kriging interpolation for each different set of geolocation errors. For each fire, we used the per-pixel s.d. of the 10 simulated progression maps as an indicator of the potential interpolation error due potential geolocation errors.

Comparison of kriging, MCD45A1 and MCD64A1 with daily fire perimeter data

The kriging maps of daily fire progression for the nine south-western fires were compared with the USFS data. The fire perimeter data were registered in a Universal Transverse Mercator grid with the World Geodetic System 1984 as geodetic datum at 500-m resolution and the kriging maps were co-registered to the same grid. To match the discrete day of the year (DOY) values of the fire perimeter data, the decimal output of the kriging results (local time, the conversion between the Coordinated Universal Time and local time was based on longitude) was floored to the nearest integer. The temporal difference (days) was calculated between the kriging map and the daily fire perimeter data for all pixels in the fire perimeter. We also compared the daily burnt area from the kriging model with the daily burnt area from the daily fire perimeter data. In a similar fashion, the approximate day of burning and the daily burnt area from the MCD45A1 and MCD64A1 burnt area products also were compared with the daily fire perimeter data. The MCD45A1 and MCD45A1 were therefore co-registered with the perimeter data. For all comparisons, we considered only the pixels that were classified as burnt by both the MCD45A1 and MCD64A1 products. Analysis of the efficacy of the MCD45A1 and MCD64A1 products in detecting burnt area is out of the scope of the current manuscript and has been examined in earlier work (Giglio *et al.* 2009; Roy and Boschetti 2009). No burnt pixels were detected by the MCD45A1 algorithm in the Big Meadow and Little Sand fires. For these fires, only the kriging maps and the MCD64A1 product were compared with the daily fire perimeter data.

Assessment of the kriging model using increased acquisitions in high latitudes

We conducted a complimentary quality assessment of the kriging interpolation method using data from higher latitude fires. All seven Alaska fires included in this study were located between 60 and 70°N latitude (Fig. 1*c*) and MODIS active fire observations were collected up to eight times per day (www-air.larc.nasa.gov/tools/predict.htm, accessed 21 October 2013). For days with four or less acquisitions containing active fire detections, all acquisitions were used as input to the interpolation model. For days that had more than four acquisitions containing active fire detections, we randomly selected four acquisitions as input to the interpolation model, and the remainder as validation data. By doing so, we mimicked the case of lower latitude fires for which there is a maximum of four MODIS acquisitions per day. We used decimal DOY values for this

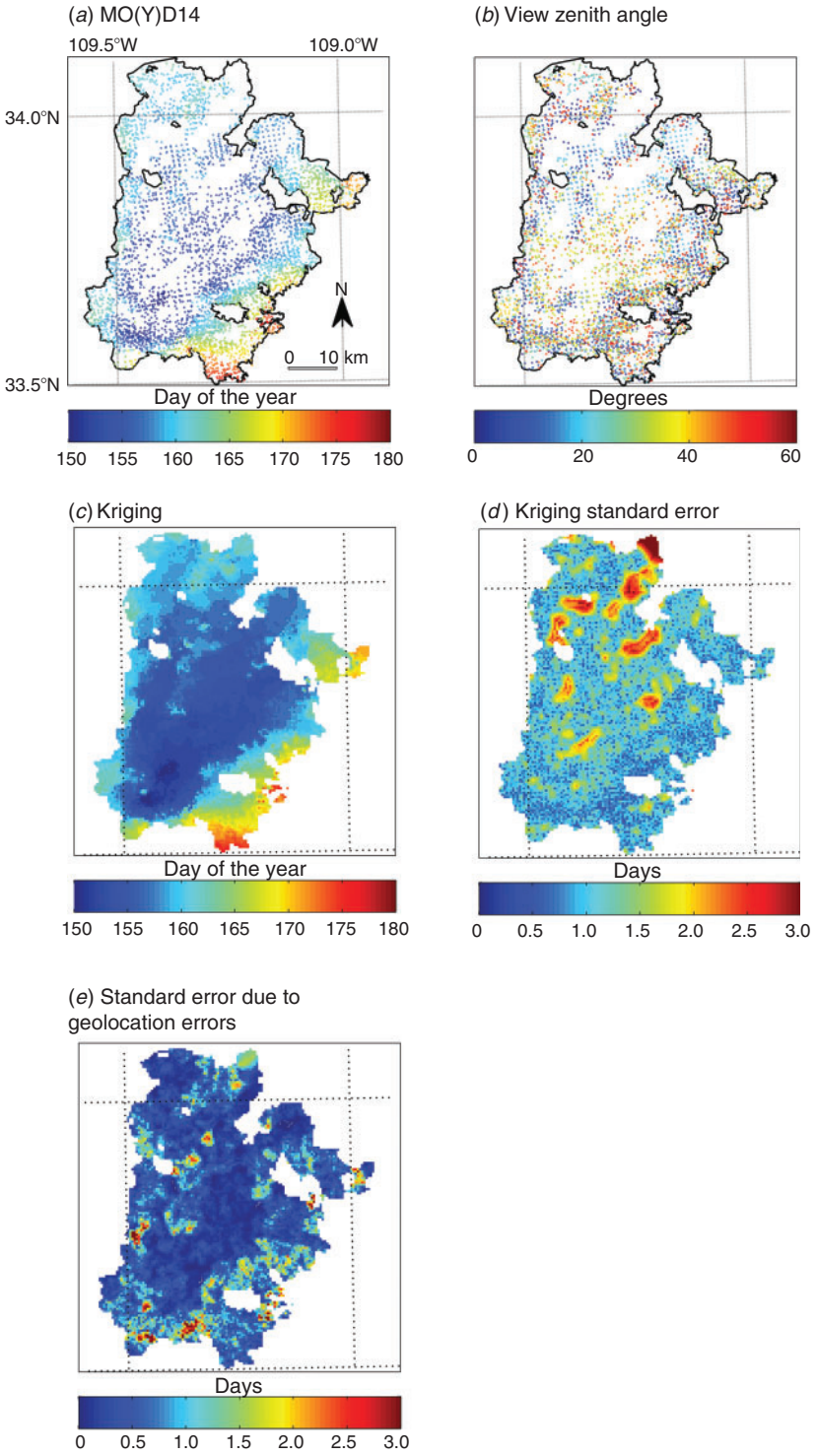

Fig. 3. Observed MO(Y)D14 active fire observations (*a*), view zenith angles (*b*), fire progression derived by kriging (*c*), kriging standard error (*d*) and standard error due to geolocation errors (*e*) for the 2011 Wallow fire in Arizona and New Mexico.

analysis. The DOY values estimated by the kriging interpolation at the location of the MO(Y)D14 observations that were used for validation were regressed against the MO(Y)D14 observations at these same locations.

Results

The kriging parameters (nugget, sill, range and number of observations included) varied across the fires studied (Table 2).

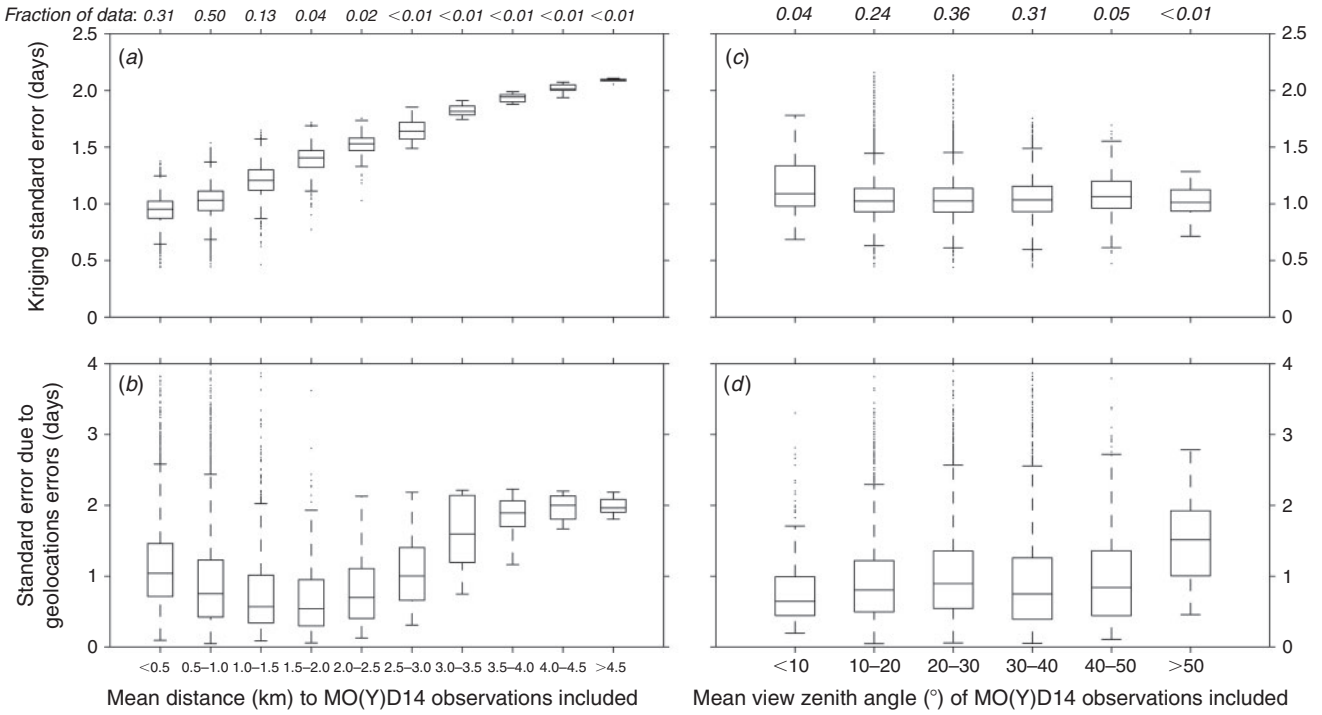

Fig. 4. Relationship between the mean distance and view zenith angle to or of the MO(Y)D14 observations included for a pixel's kriging interpolation and the kriging standard error, and the standard error due to geolocation errors. This figure is for the Wallow fire.

The spherical variogram fit yielded R^2 values between 0.67 and 0.99. Most fires did not exhibit a nugget effect, although the Station, Whitewater Baldy, Boundary, Little Black One, Pingo and Wintertrail fires had nugget values larger than 0 days^2. Sill and range values varied widely, respectively between 2 and 857 days^2 and 4 and 76 km. The number of observations included in the interpolation was between four and six for all fires. The median kriging standard error was 0.80–3.56 days, and the median standard error due to potential geolocation errors was 0.34–2.72 days.

The original MO(Y)D14 active fire observations, the view zenith angles of the MO(Y)D14 observations, the kriging map, the kriging standard error and the standard error due to geolocation uncertainties are shown in Fig. 3 for the case of the Wallow fire. The Wallow fire started at DOY 150 in 2011 from two separate ignitions that joined and quickly progressed for the first 15 days, after which the fire more slowly spread before being contained on DOY 177. The MODIS active fire detections had a discontinuous distribution in the Wallow fire perimeter, with dense areas contrasting with areas in which few fire pixels were detected. View zenith angles ranged between 0 and 55° and their distribution in the fire perimeter was evenly spread. Areas with few MODIS active fire observations were associated with higher kriging standard errors, whereas the standard error due to geolocation error tended to be higher in areas dense in active fire detections (Fig. 3). The median kriging standard error increased with increasing distance of the pixel to the MO(Y)D14 observation included (Fig. 4*a*). The median standard error due to geolocation errors was also higher with increasing distance of the pixel to the MO(Y)D14 observations included. However, for shorter distances (smaller than 2000 m) many outliers with high errors were apparent (Fig. 4*b*). The mean view zenith angle of the MO(Y)D14 observations included in the interpolation had little effect on the kriging standard error and the standard error due to geolocation error. The standard error due to geolocation error was higher when the mean view zenith angle of the MO(Y)D14 observations included was larger than 50° than when mean view zenith angles were smaller than 50° (Fig. 4*c–d*). However, mean view zenith angles larger than 50° represented only a small fraction of the data (<1%). All these pixels corresponded with outliers in areas with high densities of active fire observations that had high geolocation errors in Fig. 4*b*. The exclusive location in high density areas and the limited sample size of this class explains the observed discontinuity for the class with mean view zenith angles larger than 50° in Fig. 4*d*.

The perimeters and daily fire progression map from the USFS, along with the MCD45A1 and MCD64A1 products for the case of the Wallow fire are depicted in Fig. 5. For seven out of the nine fires, the kriging method performed better than the MCD45A1 or MCD64A1 products, whereas for the other two fires MCD64A1 had the highest level of performance (for the Big Meadow and Little Sand fires) (Fig. 6). On average, 34% of the data (s.d. = 15%) were assigned the correct DOY by the kriging interpolation across the different fires, compared with 12% (s.d. = 6%) for MCD45A1 and 21% (s.d. = 7%) for MCD64A1. Seventy-three percent (s.d. = 15%) of the data were classified within a 1-day accuracy using kriging, compared with 33% (s.d. = 15%) for MCD45A1 and 53% (s.d. = 5%) for MCD64A1 (Table 3). It is also clear from Fig. 6*j*, in which the results were averaged over the nine fires, that both MCD45A1 and MCD64A1 had a tendency to estimate later burn dates

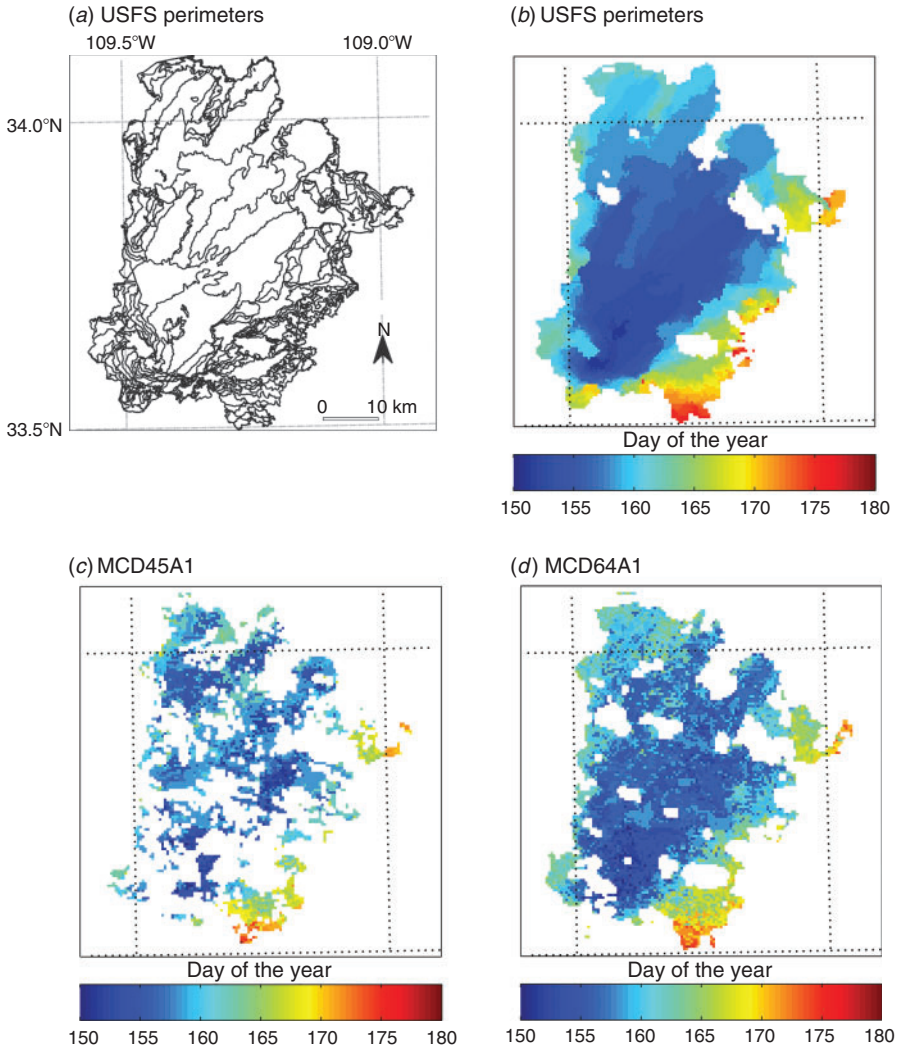

Fig. 5. Observed daily fire perimeter data from the US Forest Service (USFS) (*a*, *b*), and fire progressions maps of the MCD45A1 (*c*) and MCD64A1 (*d*) products for the 2011 Wallow fire in Arizona and New Mexico.

compared with the fire perimeter data (positive time differences in Fig. 6*j*). In addition, the kriging product had a higher percentage of the data with a temporal accuracy of less than 3 days (on average 93% according to Table 3).

For seven of the nine fires, the kriging interpolation resulted in the highest correlation ($R^2 = 0.30$–0.96) of the daily burnt area estimates as compared with the daily burnt area from the USFS fire perimeter data (Table 4). The MCD64A1 product had the highest correlation for the Horseshoe and Big Meadow fires with respective R^2 values of 0.61 and 0.84. We divided the root mean squared error (RMSE) by the sample area of the fire to normalise for sample size. This statistic gave similar trends as the R^2 values: the kriging interpolation resulted in the lowest normalised RMSE for seven fires. The MCD64A1 product scored best for the Horseshoe and Big Meadow fires and the MCD45A1 had the lowest normalised RMSE for the Station fire. Averaged over the nine fires, the kriging method had the highest R^2 ($R^2 = 0.64$, s.d. = 0.26) compared with 0.17 (s.d. = 0.23) for the MCD45A1 product and 0.47 (0.22) for the MCD64A1 product. Nonetheless, caution should be applied when interpreting these results because of the small sample sizes for several fires. This is because we only included pixels that were detected in both the MCD45A1 and MCD64A1 products.

For the Alaskan fires, the kriging interpolation provided estimates of the time of burning that closely matched the observations in many instances (Table 5). For all fires, the kriging model predicted the time of burning with R^2 values between 0.97 and ~1.0 (~1.0 for all data pooled), whereas the RMSEs were between 0.70 and 1.63 days (1.25 days for all data pooled). In addition, the mean temporal difference between the kriging estimates and the MODIS data used for validation ranged between −0.09 and 0.05 days across all seven fires (−0.01 days for all data pooled).

Discussion

The potential of the temporal information of the MODIS active fire product (Giglio *et al.* 2003) to improve our understanding of fire processes has been well recognised (Giglio 2007;

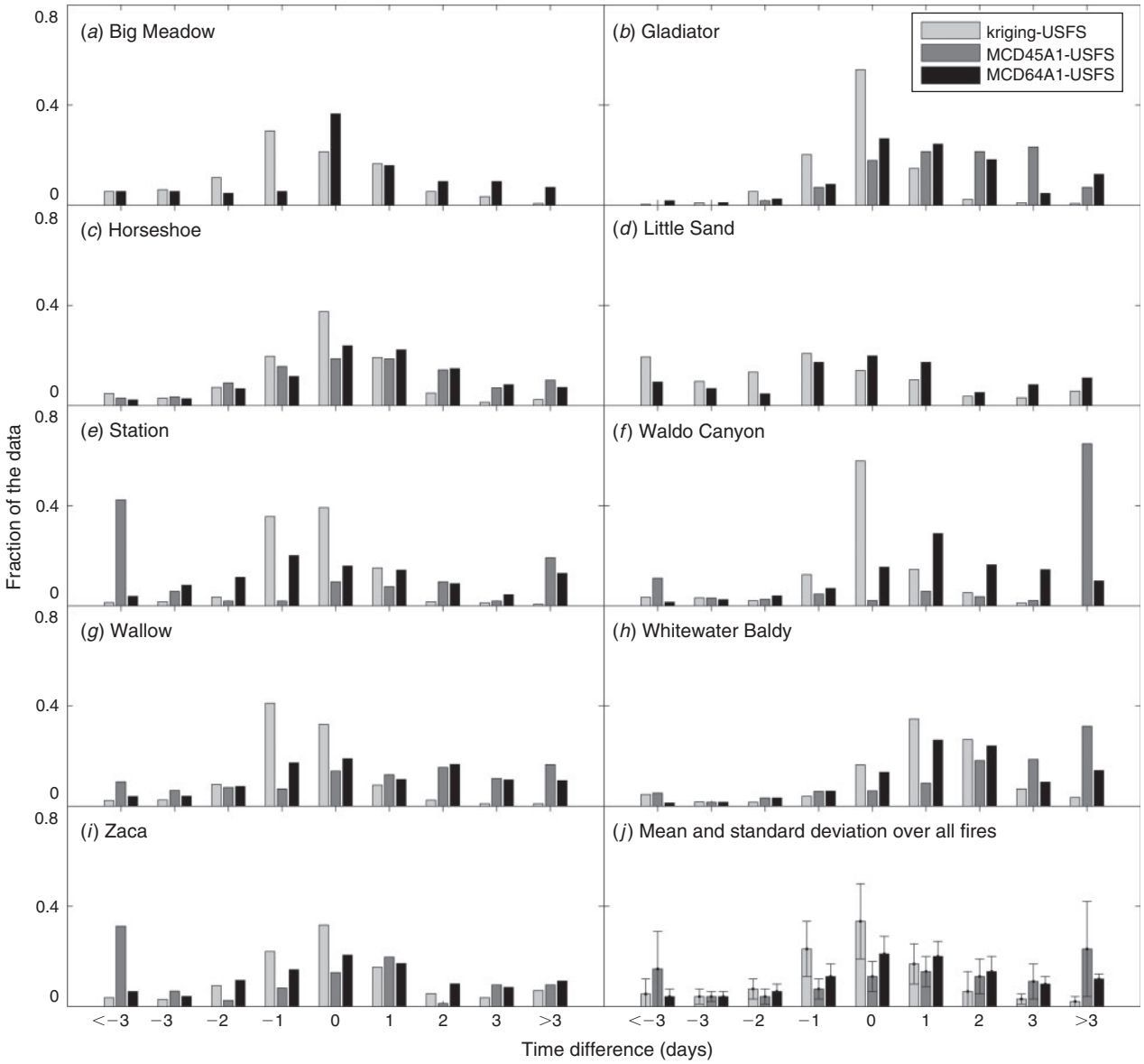

Fig. 6. Fraction of the burnt area with time differences (between <-3 and >3 in daily steps) between kriging, MDC45A1 or MCD64A1 estimates and the US Forest Service (USFS) observations for the nine fires in the south-west. Positive time differences indicate a later estimate of the day of burning compared with the USFS observations. Panel *j* gives the averages (and standard deviations as error bars) over the nine fires. (Note that the Big Meadow and Little Sand fire were not detected by the MCD45A1 algorithm and as such this product was not included for these fires). These numbers are also summarised in Table 3.

Table 3. Average (standard deviation) reporting accuracy (%) over the nine south-western fires (Fig. 1) within 0, 1, 2 or 3 days for the comparison between kriging, MCC45A1, or MCD64A1 products and daily US Forest Service (USFS) perimeter data

	0 days	1 day	2 days	3 days
Kriging–USFS	34 (15)	73 (15)	87 (10)	93 (7)
MCD45A1–USFS	12 (6)	33 (15)	49 (21)	63 (25)
MCD64A1–USFS	21 (7)	53 (5)	73 (5)	86 (3)

Loboda and Csiszar 2007; Mu *et al.* 2011; Thorsteinsson *et al.* 2011). However, within individual fire perimeters the MODIS active fire detections generally result in a discontinuous distribution with many gaps (Fig. 3*a*). This discontinuity can be partly attributed to cloud and smoke, and fire spread rates that are high compared with satellite sampling intervals. Cloud cover significantly reduces the number of active fire detections. Latitude influences the number of overpasses and their timing. Local conditions such as the distribution of fuels, fuel moisture and fire weather influence the fire spread rate.

Here we applied kriging, a well-accepted interpolation technique (Royle *et al.* 1981; Holdaway 1996), to MODIS active fire

Table 4. Slope, intercept, coefficient of determination (R^2) and root mean squared error (RMSE) normalised by sample area (the burnt area that was detected by both the MCD45A1 and MCD64A1 products) of the linear regression fits between the daily burnt area from the US Forest Service (independent variable) and the estimated daily burnt area from kriging, the MCD45A1 product and the MCD64A1 product over the nine fires in the south-west

The bold values in the R^2 and RMSE ÷ Sample area columns denote the respective highest and lowest values of the three methods compared. (Note that the Big Meadow and Little Sand fire were not detected by the MCD45A1 algorithm and as such this product was not included for these fires). s.d., standard deviation

Fire name	Sample area (ha)	Intercept			Slope			R^2			RMSE ÷ Sample area		
		kriging	MCD45A1	MCD64A1	kriging	MCD45A1	MCD64A1	kriging	MCD45A1	MCD64A1	kriging	MCD45A1	MCD64A1
Big Meadow	2855	135	–	82	0.31	–	0.68	0.27	–	**0.84**	0.068	–	**0.039**
Gladiator	1094	13	36	23	0.96	0.43	0.65	**0.96**	0.15	0.51	**0.038**	0.089	0.055
Horseshoe	47 142	352	464	353	0.63	0.53	0.64	0.59	0.30	**0.61**	**0.011**	0.017	**0.011**
Little Sand	3969	15	–	15	0.80	–	0.83	**0.62**	–	0.50	**0.016**	–	0.021
Station	1094	3	52	32	0.95	−0.01	0.41	**0.30**	~0	0.21	0.128	**0.067**	0.07
Waldo Canyon	2653	7	190	122	0.96	−0.15	0.27	**0.88**	0.02	0.19	**0.043**	0.134	0.069
Wallow	129 620	651	121	971	0.83	0.79	0.76	**0.84**	0.65	0.66	**0.016**	0.032	0.024
Whitewater Baldy	32 825	453	782	557	0.47	0.09	0.36	**0.44**	0.01	0.23	**0.034**	0.049	0.041
Zaca	1620	1	20	12	0.95	0.27	0.57	**0.84**	0.09	0.51	**0.016**	0.034	0.022
Mean (s.d.)	24 764	181	238	241	0.76	0.28	0.57	**0.64**	0.17	0.47	**0.041**	0.060	**0.039**
overall fires	(42 746)	(244)	(285)	(332)	(0.24)	(0.33)	(0.19)	(0.26)	(0.23)	(0.22)	(0.037)	(0.040)	(0.021)

Table 5. Intercept (a), slope (b), coefficient of determination (R^2) and root mean squared error (RMSE) of the linear regression fits between the day of the year kriging on the location of the MO(Y)D14 validation data (dependent variable) *v.* the day of the year from the MO(Y)D14 validation data (independent variable) for the seven fires in Alaska

The results of the regression were the pooled data from all fires are also provided. The mean difference is defined as the day of the year of the MO(Y)D14 validation data minus the day of the year estimated by kriging on the location of the MO(Y)D14 validation data. (n = the number of points in the validation dataset)

Fire name	n	Mean difference (days)	a	b	R^2	RMSE (days)
Boundary	1516	0.04	1.82	0.99	~1	1.03
Dall City	2422	~0	3.54	0.98	0.99	0.99
Little Black One	1521	−0.08	8.54	0.96	0.97	1.63
Minto Flats South	1644	0.04	3.49	0.98	0.99	1.00
North Dag	501	0.05	1.04	0.99	~1	0.70
Pingo	2214	−0.02	1.76	0.99	~1	1.42
Wintertrail	1817	−0.09	3.41	0.98	0.99	1.43
All fires	11 635	−0.01	1.41	0.99	~1	1.25

observations to create continuous fire progression maps at moderate-resolution scale (500 m). Kriging uses local information in a spatial interpolation model. The local information as represented by spatial distribution of the MODIS active fire overpass times was quantified by a variogram fit for each fire. The two main reasons why we chose kriging as an interpolation technique are that it (1) is based on local variogram analysis, which is used to parameterise the interpolation model, and (2) allows an uncertainty analysis by spatially estimating the kriging standard error (Holdaway 1996). Other and less complex interpolation models such as inverse distance weighting (Watson and Philip 1985) may also be very useful for mapping fire progression based on active fire data. For example, preliminary tests demonstrated that inverse distance weighting achieved similar performances as kriging when compared with the USFS observations.

The kriging error depends on the variogram parameters and the pixel's distance to the active fire observations included in the interpolation. Naturally, the kriging error increased with increasing distance to the active fire observations (Figs 3*c*, 4*a*). In contrast, the highest errors due to potential geolocation errors were found in areas with a high density of active fire observations (Figs 3*e*, 4*b*). Dense active fire areas are the result of a slow-moving fire front. In these areas, small variations in the geolocation of the active fire observations can result in significant errors. Given that the fire front moved slowly in these areas, a distribution of active fire observations with widely varying scan angles can influence the location of individual observations, and subsequently affect the resulting prediction of the time of burning. In contrast, in many areas with few active fire observations, often as a result of a fast-moving fire front, small variations in geolocation have little influence on which observations are included in the interpolation, and thus have little effect on estimates of burning. The increasing sub-pixel geolocation

uncertainty with increasing view zenith angles is likely the most important error source of the interpolation analysis and might be reduced in future work by modifying the selection criteria for active fires in dense clusters (i.e. modify the kriging algorithm to select low scan angle observations in high density regions). The co-registration between the fire perimeter data, the kriging results, and the MCD45A1 and MCD64A1 products may introduce additional sources of error in our comparisons. The MODIS point spread function (PSF) may introduce additional noise in the interpolation model. As a result of the MODIS PSF, the spectral response of a pixel is determined not only by the area from the pixel itself but also by adjacent areas (Wolfe *et al.* 2002). This creates partial overlap between neighbouring pixels and may result in the same thermal anomaly being detected more than once.

Averaged over the nine south-west fires, the kriging interpolation demonstrated a within-1-day accuracy of 73%, which outperformed the temporal accuracies of the day of burning reported by the MCD45A1 and MCD64A1 products (Table 3). In addition, a regression analysis over seven Alaska fires resulted in RMSEs between 0.70 and 1.63 days (Table 5). The kriging interpolation over the Alaska fires only used four out of eight MODIS acquisitions per day to mimic the MODIS acquisition scheme at lower latitude locations. Therefore, even better performances can be expected for higher latitude fires if all data are included in the kriging interpolation. The accuracy of the kriging progression models will thus depend on the latitude of the fire location. The interpolation will benefit from more daily acquisitions by MODIS at higher latitudes, and possibly in the future from a combination of Visible Infrared Imager Radiometer Suite (VIIRS) and MODIS observations.

The MCD45A1 and MCD64A1 products showed a tendency to predict later burn dates than the USFS observations (Fig. 6*j*). This time delay may occur because both products use post-fire reflectance changes in their algorithm to detect the burning and assign the date of burning. Any gap in surface reflectance from incomplete satellite coverage or smoke or cloud cover will create a larger interval spanning the burn date. In addition, differences in the way the USFS daily fire perimeter data were collected compared with the functioning of the active fire and burnt area algorithms may explain some of this bias. For example, it is likely that the USFS perimeters span across different areas that have burnt incompletely, because the outer perimeter is probably the most critical variable of interest for fire managers attempting to design containment strategies. The active fire and burnt area products, in contrast, will record thermal anomalies (and burnt areas) at later times as gaps within the outer perimeter are subsequently burnt by infilling.

In a global accuracy assessment of the day of burning reported by the MCD45A1 product, Boschetti *et al.* (2010) found that 50% of the burnt area detections occurred within the accuracy of a single day. We found that 34% of the burnt pixels within the MCD45A1 product were assigned the date within a single-day accuracy, when averaged over the nine fires over the south-western US in this study (Table 3). Although the fires included in this study occurred in different ecosystems including grassland, shrubland and coniferous forest, the overall accuracy depends on the selected study areas and thus we do not expect our accuracy assessment to necessarily agree with those conducted on other regions, including the one reported by Boschetti *et al.* (2010). It is also important to note that the temporal accuracy for the majority of the pixels detected by the MCD45A1 product (Table 2) was considerably better than the nominal uncertainty of 8 days as reported by Roy *et al.* (2005). The higher performance of the MCD64A1 compared with MCD45A1 may originate from the synergetic use of post-fire reflectance changes and active fire detections in MCD64A1.

Fire spread is largely governed by fuel availability, topography and weather (Finney 2001, 2003). Fuel types, distribution, density and moisture content are critical to a landscape's capacity to carry fire (Papadopoulos and Pavlidou 2011). The fuel moisture content is determined by both a long-term effect of pre-fire weather, as well as the weather during the fire event (Pereira *et al.* 2005). Fire occurrence is favoured by low humidity and high temperature, whereas wind speed has long been recognised as the crucial factor influencing the rate of spread of wildfires (Rothermel 1972; Fosberg 1978). In addition, interactions of fuels and weather with local topography can greatly influence fire activity (Moritz *et al.* 2010; Sharples *et al.* 2012). Fire behaviour models incorporate information on fuels, topography and weather to predict fire spread (Sullivan 2009*a*, 2009*b*, 2009*c*). Comparison of fire behaviour model outcomes against real-world fires has indicated that models typically do not accurately predict fire progression (Papadopoulos and Pavlidou 2011; Finney *et al.* 2013). Our method to map fire progression based on remote sensing observations provides an independent information source to assess the performance of fire spread models. In addition, fire progression maps derived from remote sensing can be used to revisit relationships between environmental controls (fuels, topography and weather) and fire spread rates across different ecosystems, and as such they can contribute to improved fire behaviour models. Another application of fire progression maps lies within the bottom-up calculation of wildfire emission models which quantify the burnt area, fuel load, combustion completeness and emission factors. Fuel load, combustion completeness and emission factors fluctuate on short temporal scales (Boschetti *et al.* 2010; van Leeuwen and van der Werf 2011). Current wildfire emission models, however, use fixed values for these variables throughout the whole fire scar or operate with a coarse temporal resolution (van der Werf *et al.* 2010; French *et al.* 2011). Detailed temporal information on fire progression may allow daily weather data to be incorporated into fuel load, combustion completeness and emission factor estimates. This would reduce uncertainties in these variables and associated emissions.

Conclusions

This study presented a kriging interpolation to construct continuous fire progression maps from MODIS active fire data at a moderate spatial scale (500 m). Overall, the kriging interpolation mapped 73% of the area burnt within the accuracy of a single day and outperformed the two existing MODIS burnt area products. Spatially explicit temporal wildfire emissions are a critical input for a variety of applications such as regional air transport models. Temporal information on burnt area progression is also important to allow temporal bottom-up inventories of wildfire emissions. In addition, fuel load and

combustion completeness estimates generally require weather inputs to account for the fuel moisture content. Fire progression maps allow these variables to vary temporally instead of assuming a fixed value for the whole fire event. Fire progression maps also permit studying the environmental controls such as fire weather and fuel distributions on fire behaviour and characteristics. The method presented here has potential for improving fire emissions estimates and for validating and constructing better fire behaviour models.

Acknowledgements

The research described in this paper was carried out at the Jet Propulsion Laboratory, California Institute of Technology, under a contract with the National Aeronautics and Space Administration. The work was funded by a NASA grant for Interdisciplinary Research in Earth Science (NNX10AL14G). We thank Lorri Peltz-Lewis and Thomas Mellin of the USFS for granting us access to the perimeter data of the fires in the southwest included in this study. We are also grateful to the fire personnel who created the fire perimeter data. Work performed in this study was conducted on official time so any research or applications arising from this remain under copyright of California Institute of Technology. Government sponsorship acknowledged.

References

Boschetti L, Roy D, Justice C, Giglio L (2010) Global assessment of the temporal reporting accuracy and precision of the MODIS burned area product. *International Journal of Wildland Fire* **19**, 705–709. doi:10.1071/WF09138

Chuvieco E, Martin M (1994) A simple method for fire growth mapping using AVHRR channel 3 data. *International Journal of Remote Sensing* **15**, 3141–3146. doi:10.1080/01431169408954316

Cisneros R, Schweizer D, Zhong S, Hammond K, Perez M, Guo Q, Traina S, Bytnerowicz A, Bennett D (2012) Analysing the effects of the 2002 McNally fire on air quality in the San Joaquin valley and southern Sierra Nevada, California. *International Journal of Wildland Fire* **21**, 1065–1075. doi:10.1071/WF11025

Finney M (2001) Design of regular landscape fuel treatment patterns for modifying fire growth and behavior models. *Forest Science* **47**, 219–228.

Finney M (2003) Calculation of fire spread rates across random landscapes. *International Journal of Wildland Fire* **12**, 167–174. doi:10.1071/WF03010

Finney M, Cohen J, McAllister S, Jolly W (2013) On the need for a theory of wildland fire spread. *International Journal of Wildland Fire* **22**, 25–36. doi:10.1071/WF11117

Fosberg M (1978) Weather in wildland fire management: the fire weather index. In 'Proceedings of the Conference on Sierra Nevada Meteorology',19–21 June 1978, South Lake Tahoe, CA. pp. 1–4. (American Meteorological Society and USDA Forest Service: Boston, MA')

French N, de Groot W, Jenkins L, Rogers B, Alvarado E, Amiro B, de Jong B, Goetz S, Hoy E, Hyer E, Keane R, Law B, McKenzie D, McNulty S, Ottmar R, Perez-Salicrup D, Randerson J, Robertson K, Turetsky M (2011) Model comparisons for estimating carbon emissions from North American wildland fire. *Journal of Geophysical Research* **116**, G00K05. doi:10.1029/2010JG001469

Friedl M, Sulla-Menashe D, Tan B, Schneider A, Ramankutty N, Sibley A, Huang X (2010) MODIS Collection 5 global land cover: algorithm refinements and characterization of new datasets. *Remote Sensing of Environment* **114**, 168–182. doi:10.1016/J.RSE.2009.08.016

Giglio L (2007) Characterization of the tropical diurnal fire cycle using VIRS and MODIS observations. *Remote Sensing of Environment* **108**, 407–421. doi:10.1016/J.RSE.2006.11.018

Giglio L, Descloitres J, Justice C, Kaufman Y (2003) An enhanced contextual fire detection algorithm for MODIS. *Remote Sensing of Environment* **87**, 273–282. doi:10.1016/S0034-4257(03)00184-6

Giglio L, Csiszar I, Justice C (2006) Global distribution and seasonality of active fires as observed with the Terra and Aqua Moderate Resolution Imaging Spectroradiometer (MODIS) sensors. *Journal of Geophysical Research* **111**, G02016. doi:10.1029/2005JG000142

Giglio L, Loboda T, Roy D, Quayle B, Justice C (2009) An active-fire based burned area mapping algorithm for the MODIS sensor. *Remote Sensing of Environment* **113**, 408–420. doi:10.1016/J.RSE.2008.10.006

Holdaway M (1996) Spatial modeling and interpolation of monthly temperature using kriging. *Climate Research* **6**, 215–225. doi:10.3354/CR006215

Ichoku C, Kaufman Y (2005) A method to derive smoke emission rates from MODIS fire radiative energy measurements. *IEEE Transactions on Geoscience and Remote Sensing* **43**, 2636–2649. doi:10.1109/TGRS.2005.857328

Johnston F, Henderson S, Chen Y, Randerson J, Marlier M, DeFries R, Kinney P, Bowman D, Brauer M (2012) Estimated global mortality attributable to smoke from landscape fire. *Environmental Health Perspectives* **120**, 695–701. doi:10.1289/EHP.1104422

Justice C, Giglio L, Korontzi S, Owens J, Morisette J, Roy D, Descloitres J, Alleaume S, Petitcolin F, Kaufman Y (2002) The MODIS fire products. *Remote Sensing of Environment* **83**, 244–262. doi:10.1016/S0034-4257(02)00076-7

Kasischke E, Hoy E (2012) Controls on carbon consumption during Alaskan wildland fires. *Global Change Biology* **18**, 685–699. doi:10.1111/J.1365-2486.2011.02573.X

Loboda T, Csiszar I (2007) Reconstruction of fire spread within wildland fire events in Northern Eurasia from the MODIS active fire product. *Global and Planetary Change* **56**, 258–273. doi:10.1016/J.GLOPLACHA.2006.07.015

Moritz M, Moody T, Krawchuk M, Hughes M, Hall A (2010) Spatial variation in extreme winds predicts large wildfire locations in chaparral ecosystems. *Geophysical Research Letters* **37**, L04801. doi:10.1029/2009GL041735

Mu M, Randerson J, van der Werf G, Giglio L, Kasibhatla P, Morton D, Collatz G, DeFries R, Hyer E, Prins E, Griffith D, Wunch D, Toon G, Sherlock V, Wennberg P (2011) Daily and 3-hourly variability in global fire emissions and consequences for atmospheric model predictions of carbon monoxide. *Journal of Geophysical Research* **116**, D24303. doi:10.1029/2011JD016245

Papadopoulos G, Pavlidou F (2011) A comparative review on wildfire simulators. *IEEE Systems Journal* **5**, 233–243. doi:10.1109/JSYST.2011.2125230

Pereira J, Sa A, Sousa A, Silva J, Santos T, Carreiras J (1999) Spectral characterization and discrimination of burnt areas. In 'Remote Sensing of Large Wildfires in the European Mediterranean Basin'. (Ed. E Chuvieco) pp. 123–138. (Springer-Verlag: Berlin)

Pereira M, Trigo R, da Camara C, Pereira J, Leite S (2005) Synoptic patterns associated with large summer forest fires in Portugal. *Agricultural and Forest Meteorology* **129**, 11–25. doi:10.1016/J.AGRFORMET.2004.12.007

Prins E, Feltz J, Menzel W, Ward D (1998) An overview of GOES-8 diurnal fire and smoke results for SCAR-B and the 1995 fire season in South America. *Journal of Geophysical Research* **103**, 31 821–31 835. doi:10.1029/98JD01720

Rothermel R (1972) A mathematical model for predicting fire spread in wildland fuels. USDA Forest Service, Intermountain Forest and Range Experiment Station, Research Paper INT-115. (Ogden, UT)

Roy D, Boschetti L (2009) Southern Africa validation of the MODIS, L3JRC and GlobCarbon burned-area products. *IEEE Transactions on Geoscience and Remote Sensing* **47**, 1032–1044. doi:10.1109/TGRS.2008.2009000

Roy D, Lewis P, Justice C (2002) Burned area mapping using multi-temporal moderate spatial resolution data-a bi-directional reflectance model-based expectation approach. *Remote Sensing of Environment* **83**, 263–286. doi:10.1016/S0034-4257(02)00077-9

Roy D, Jin Y, Lewis P, Justice C (2005) Prototyping a global algorithm for systematic fire-affected area mapping using MODIS time series data. *Remote Sensing of Environment* **97**, 137–162. doi:10.1016/J.RSE.2005.04.007

Royle A, Clausen F, Frederiksen P (1981) Practical universal kriging and automatic contouring. *Geoprocessing* **1**, 377–394.

Schwendel A, Fuller I, Death R (2012) Assessing DEM interpolation methods for effective representation of upland stream morphology for rapid appraisal of bed stability. *River Research and Applications* **28**, 567–584. doi:10.1002/RRA.1475

Sharples J, McRae R, Wilkens S (2012) Wind terrain effects on the propagation of wildfires in rugged terrain: fire channeling. *International Journal of Wildland Fire* **21**, 282–296. doi:10.1071/WF10055

Sullivan A (2009*a*) Wildland surface fire spread modelling, 1990–2007. 1. Physical and quasi-physical models. *International Journal of Wildland Fire* **18**, 349–368. doi:10.1071/WF06143

Sullivan A (2009*b*) Wildland surface fire spread modelling, 1990–2007. 2. Empirical and quasi-empirical models models. *International Journal of Wildland Fire* **18**, 369–386. doi:10.1071/WF06142

Sullivan A (2009*c*) Wildland surface fire spread modelling, 1990–2007. 3. Simulation and mathematical analogue models. *International Journal of Wildland Fire* **18**, 387–403. doi:10.1071/WF06144

Thorsteinsson T, Magnusson B, Gudjonsson G (2011) Large wildfire in Iceland in 2006: size and intensity estimates from satellite data. *International Journal of Remote Sensing* **32**, 17–29. doi:10.1080/01431160903439858

Trigg S, Flasse S (2001) An evaluation of different bi-spectral spaces for discriminating burned shrub-savannah. *International Journal of Remote Sensing* **19**, 3499–3514.

van der Werf G, Randerson J, Giglio L, Collatz G, Kasibhatla P, Arellano A (2010) Global fire emissions and the contribution of deforestation, savanna, forest, agricultural and peat fires (1997–2009). *Atmospheric Chemistry and Physics* **10**, 11 707–11 735. doi:10.5194/ACP-10-11707-2010

van Leeuwen T, van der Werf G (2011) Spatial and temporal variability in the ratio of trace gases emitted from biomass burning. *Atmospheric Chemistry and Physics* **11**, 3611–3629. doi:10.5194/ACP-11-3611-2011

Watson D, Philip G (1985) A refinement of inverse distance weighted interpolation. *Geo-processing* **2**, 315–327.

Wolfe R, Nishihama M, Fleig A, Kuyper J, Roy D, Storey J, Patt S (2002) Achieving sub-pixel geolocation accuracy in support of MODIS land science. *Remote Sensing of Environment* **83**, 31–49. doi:10.1016/S0034-4257(02)00085-8